Multi-line Boltzmann regression for near-electronvolt temperature and CO sensing via MHz-rate infrared laser absorption spectroscopy

Nicolas Minesi, Miles Richmond, Christopher Jelloian, Nicholas Kuenning, Anil Nair, R. Mitchell Spearrin

Applied Physics B: Lasers and Optics manuscript No.
(will be inserted by the editor)

Multi-line Boltzmann regression for near-electronvolt temperature and CO sensing via MHz-rate infrared laser absorption spectroscopy

Nicolas Q. Minesi, Miles O. Richmond, Christopher C. Jelloian, Nicholas M. Kuenning, Anil P. Nair, R. Mitchell Spearrin

Department of Mechanical and Aerospace Engineering, University of California, Los Angeles (UCLA), CA 90095, USA

Received: XXXX / Revised version: XXXX

Abstract A mid-infrared laser absorption technique is developed for sensing of temperature and carbon monoxide (CO) number density from 2000 K to above 9000 K. To resolve multiple rovibrational lines, a distributed-feedback quantum cascade laser (DFB-QCL) is modulated across 80% of its current range using a trapezoidal waveform via a bias-tee circuit. The laser attains a spectral scan depth of 1 cm^{-1}, at a scan frequency of 1 MHz, which allows for simultaneous measurements of four isolated CO transitions near 2011 cm^{-1} (4.97 µm) with lower-state energies spanning 3,000 to 42,000 cm^{-1}. The number density and temperature are calculated using a Boltzmann regression of the four population fractions. This method leverages the information contained in each transition and yields a lower uncertainty than using a single line pair. The sensor is validated in shock tube experiments over a wide range of temperatures and pressures (2300–8100 K, 0.3–3 atm). Measurements behind reflected shock waves are compared to a kinetic model of CO dissociation up to 9310 K and are shown to recover equilibrium conditions. The high temperature range of the sensor is able to resolve rapid species and temperature evolution at near electronvolt conditions making it suitable for investigations of high-speed flows, plasma applications, and high-pressure detonations.

1 Introduction

1.1 Background

Accurate and precise measurements of the thermodynamic state in combustion and plasma applications are necessary to optimize performance and understand key processes. Extreme temperatures occur frequently in combustion where, for instance, a practical rocket engine burning CH_4:O_2 at 300 bar reaches 3800 K in the combustion chamber, while detonating fuel-rich C_2H_4:O_2 mixed at 300 K and 10 atm attains 4900 K [1, 2]. Higher temperatures up to 10,000 K are obtained in industrial plasma torches [3], arc-jets [4], continuous arc discharges utilized for carbon nanotube synthesis [5, 6], and transient discharges for ignition of internal combustion engines [7, 8]. Shorter-duration arc-type discharges of several nanoseconds, employed notably for research on CO_2 conversion and plasma-assisted combustion, can present core temperatures from 1000s to 10,000s of kelvin [8–12]. Finally, hypersonic flows generate shock layers with temperatures in the range of 5000–10,000 K during planetary entry [13, 14]. These complex environments must be accurately characterized to inform mass-efficient thermal protection system design [15, 16].

At such extreme near-electronvolt temperatures, most physical sensors are not able to survive the associated heat flux and optical methods must be employed for in-situ detection. Within the multitude of environments aforementioned, carbon monoxide (CO) is commonly generated via oxidation of carbon or dissociation of CO_2, rendering CO an attractive optical target for gas measurements. Prior sensing of CO concentration and temperature above 3500 K has involved optical emission spectroscopy (OES), demonstrated in arc-like discharges [8–12], plasma torches [15, 17], and shock tubes [16, 18, 19]. Emission diagnostics are well-suited to probe highly radiative sources but require optical calibration for quantitative interpretation, particularly for speciation. Laser absorption spectroscopy (LAS) can be calibration-free and highly quantitative, which makes it a valuable complement to OES at high temperatures. Recent advances in laser tuning rates have further enabled MHz-rate LAS sensing, providing the capability to resolve high-temperature chemistry occurring at microsecond timescales [20].

1.2 High-speed laser absorption spectroscopy

Prior advances in high-temperature CO sensing provide a basis for the current work. CO measurements in the

3500–4000 K range were reported in shock-tube environments using LAS [21, 22]. These sensors were designed for combustion applications, with diminishing sensitivity above 4000 K and a time resolution inadequate for higher temperature kinetics. In that context, single-line scanned LAS was developed for CO number density sensing at 100 kHz up to 8000 K, but OES measurements were needed to determine the temperature [19]. In another work, MHz single-line scanned LAS of CO demonstrated temperature measurements (2500–10,000 K) using Doppler broadening [18, 23–25]. This approach probes the translational temperature from the Doppler linewidth, but loses sensitivity at modest pressures when collisional broadening becomes substantial [18, 23–25]. These shortcomings could be circumvented using several optical transitions during one scan, the relative intensities of which depend on temperature according to the Boltzmann distribution. However, when scanning at frequencies above 10–100 kHz to track fast chemistry occurring at these temperatures, the available spectral scan-depth of tunable semiconductor lasers is reduced, such that only a single spectral feature can typically be resolved. Recent efforts by our research group have shown this tuning limitation can be overcome with bias tee circuitry and waveform optimization.

In [20, 26], a bias tee circuit was employed to diplex DC current generated from a laser controller with an RF modulation signal (AC), effectively bypassing the current controller bandwidth limitation (typically around 200 kHz). This modulation scheme, illustrated in Fig. 7, increased the scan-depth by one order of magnitude, sufficient to capture multiple rovibrational transitions of CO and CO_2 at several MHz [20]. This type of bias-tee circuit, modulated at high speeds, has also been employed in several entry-related studies where µs time resolution was needed [27–29].

Further scan-depth improvement was achieved more recently by scanning DFB lasers below the lasing threshold and employing a squared current waveform modulation [30]. This type of modulation increased the temperature variations experienced by the laser chip within one scan and multiplied the spectral scan depth by more than 2 compared to a sine wave modulation. Ultimately, these combined improvements resulted in a scan depth of 1 cm^{-1} at 1 MHz. This second recent advance in laser tunability fostered the development of a new CO multi-line scanned-wavelength LAS sensor presented in this work, able to perform accurate number density and temperature measurements at 1 MHz and in the range 2000–9000 K.

Before discussing the sensor performance, the absorption spectroscopy approach and data processing methods are presented in Section 2. In Section 3, the experimental setup is described. In Section 4, the sensor validation and demonstration with chemically frozen high-temperature CO mixtures is discussed. Finally, in Section 5, we compare the species and temperature measurements of shock-heated CO with equilibrium values and a kinetic simulation. In Appendix A, a detailed uncertainty analysis useful for line selection is conducted. In Appendix C, the robustness of the present line selection is assessed in the case of non-uniform path-integrated temperatures.

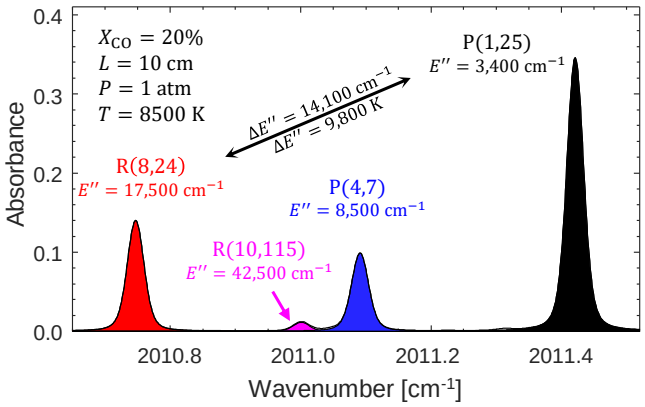

Fig. 1 Simulated spectrum of CO on the 1-cm^{-1} range employed in this work with the four major lines indicated by filled areas.

2 Methods

2.1 Line selection and line pair comparison

The methods and principles of laser absorption spectroscopy are extensively discussed in [31]. The absorbance α_i of a single line can be calculated using the incident and transmitted light intensities I_0 and I_t, respectively:

$$\alpha(\nu) = -\ln\left(\frac{I_t}{I_0}\right)_\nu \tag{1}$$

For a uniform gas, the Beer-Lambert law relates the spectrally-integrated absorbance area, A_i, of a single spectral feature, i, to the CO number density, n_{CO} [cm^{-3}], the optical pathlength, L [cm], and the linestrength, S_i [$cm^{-1}/(molec{\cdot}cm^{-2})$], at the gas temperature, T [K]:

$$\int_\nu \alpha_i(\nu)d\nu = A_i = n_{CO}LS_i(T) \tag{2}$$

The transition lineshapes are approximated by a Voigt function. The Voigt lineshape is a convolution of the Gaussian and Lorentzian functions and is calculated using the polynomial approximation of McLean [32].

In previous works [20, 28], CO mole fraction and temperature were measured using the P(2,20) and P(0,31) transitions near 2008 cm^{-1}. In this section, we show that accounting for the sensitivity of the line areas to temperature and CO mole fraction, the 2010.6–2011.6 cm^{-1} spectral region, presented in Fig. 1, is favorable for temperatures above 2000 K. The linestrengths of these transitions are shown in Fig. 2. The complete derivation of

Table 1 HITEMP2019 spectroscopic data of the four main transitions utilized in this work (truncated values) with linestrength uncertainties given in brackets [33]

Transition	ν, cm^{-1}	S_i^0, cm	E'', cm^{-1}
R(8,24)	2010.746	$2.50 \cdot 10^{-54}$ [5-10%]	17475.86
R(10,115)	2011.000	$2.23 \cdot 10^{-106}$ [≥20%]	42479.85
P(4,7)	2011.091	$3.20 \cdot 10^{-36}$ [5-10%]	8518.19
P(1,25)	2011.421	$3.26 \cdot 10^{-25}$ [1-2%]	3378.95

the temperature and mole fraction uncertainty is provided in Appendix A and only the key points are presented here. The ratio of areas of two lines, R, is equal to the ratio of their linestrengths, solely a function of the temperature, T.

$$\frac{A_i}{A_j} = \frac{S_i(T)}{S_j(T)} = R(T) \tag{3}$$

After differentiation of Eq. 3 and manipulation of this equation, the temperature uncertainty is given by:

$$\frac{\delta T}{T} = \frac{k_B}{hc}\frac{T}{\Delta E}\sqrt{\sum_{i=1}^{2}\left[\left(\frac{\delta S_i^0}{S_i^0}\right)^2 + \left(\frac{1}{\mathrm{SNR}}\frac{\exp\left(\alpha_i^{\mathrm{pk}}\right)}{\alpha_i^{\mathrm{pk}}}\right)^2\right]} \tag{4}$$

where k_B is the Boltzmann constant, h, the Planck constant, c, the speed of light, δS_i^0, the room-temperature linestrength uncertainty of line i, and α_i^{pk}, its peak absorbance. The spectroscopic constants of the four main transitions in the 2010.6–2011.6 cm^{-1} spectral region are given in Table 1. In this work, the signal-to-noise ratio reaches SNR $\sim$ 440, using the root mean square noise of the raw measurement voltage, $U_{\mathrm{noise}} \sim 4.5$ mV, and the background amplitude voltage, $U_0 \sim 2$ V. As expected, a high SNR is desirable, because it will increase confidence in the measurement of the line areas, which reduces the uncertainty in the temperature measurement based on the ratio of these areas. The term $\exp\left(\alpha_i^{\mathrm{pk}}\right)/\alpha_i^{\mathrm{pk}}$ reaches a minimum around $\alpha_i^{\mathrm{pk}} = 1$. Effectively, this term indicates that the lowest line area uncertainty is reached when the peak absorbance is approximately 1. The function $\exp\left(\alpha_i^{\mathrm{pk}}\right)/\alpha_i^{\mathrm{pk}}$ is above 5 for a peak absorbance outside the range 0.3–2.6, which mathematically shows that a spectrum that is too optically thick or thin should be avoided when possible. Finally, it should be noted that for any line pair selection, the uncertainty in the temperature measurement increases with T due to the $T/\Delta E$ factor. This increase can be compensated by choosing two lines with a high difference in their ground-state energies E''.

The number density can be derived from the Beer-Lambert law (Eq. 2).

$$n_{\mathrm{CO}} = \frac{A_i}{L S_i(T)} \tag{5}$$

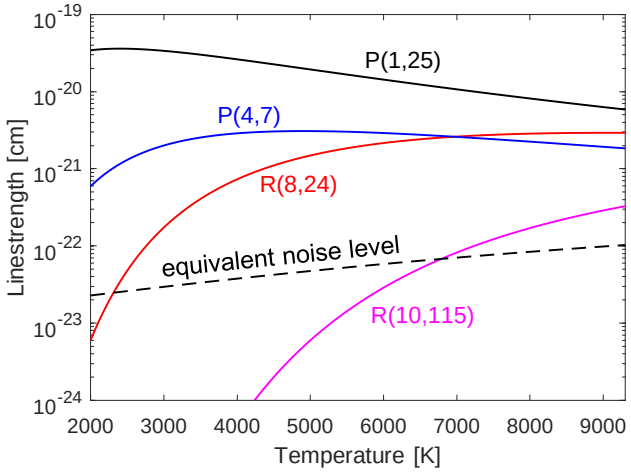

Fig. 2 Linestrengths versus temperature of the strongest transitions in the 2010.6 - 2011.6 cm^{-1} region (∼4.97 µm). The equivalent noise level is estimated using a rectangular area, $\delta\alpha = 0.003$, $L = 10$ cm, P = 1 atm, and $X_{\mathrm{CO}} = 10\%$.

The differentiation of Eq. 5 detailed in the Appendix A provides the number density uncertainty in Eq. 6:

$$\left(\frac{\delta n}{n}\right)^2 = \left(\frac{1}{\mathrm{SNR}}\frac{\exp\left(\alpha_i^{\mathrm{pk}}\right)}{\alpha_i^{\mathrm{pk}}}\right)^2 + \left(\frac{\delta L}{L}\right)^2 + \left(\frac{\partial S}{\partial T}\delta T\right)^2 + \left(\frac{\delta S_i^0}{S_i^0}\right)^2 \tag{6}$$

This expression contains similar factors to the temperature uncertainty, with the addition of the linestrength derivative with respect to T, $\partial S/\partial T$, and the pathlength uncertainty $\delta L/L = 1\%$.

In Fig. 3, the variation of $\delta T/T$ for four line pairs is given as a function of temperature. These expressions are evaluated for a pathlength and a pressure representative of our conditions ($L = 10.32$ cm, $X_{\mathrm{CO}} = 10\%$, and $P = 1$ atm), but can be easily applied to other conditions. The previous line selection used by our group near 2008 cm^{-1}, P(0,31)/P(2,20), is shown in black for 2% and 10% mole fractions. At 2% concentration, these lines show their best temperature sensitivity in the 1000–4000 K region, where they were used previously [20, 28]. However, above this range, their sensitivity decreases because their peak absorbance decreases. Using a CO mole fraction of 10%, this line pair can be used at higher temperatures but its sensitivity still degrades above 5000 K. Note that a neighboring line, P(3,14), is blended with P(0,31). Although the perturbation induced by the P(3,14) line can be taken into account, it can also add another contribution to the uncertainty analysis, see Section A.3. Therefore, in this work, we use the region 2010.6–2011.6 cm^{-1} to probe the P(1,25), R(10,115), P(4,7), and R(8,24) transitions that are spectrally isolated from each other. The R(10,115) / P(1,25) line pair presents the largest energy difference, $\Delta E'' \approx 39,000$ cm^{-1}, but cannot be used

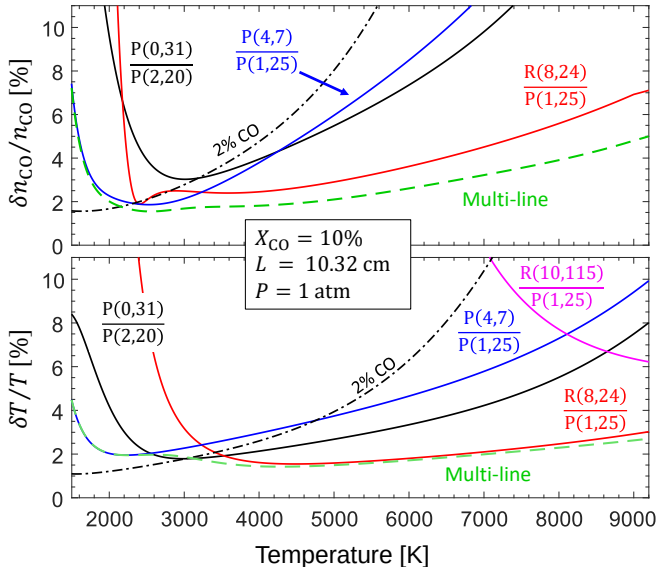

Fig. 3 Relative temperature and number density uncertainty for given line ratios, calculated for a 10% CO mole fraction. The multi-line fit, in green, presents lower uncertainty than individual line pairs. The line pair used in previous works [20, 29] is shown in black at 2% and 10% CO mole fraction to highlight the different range of application of each line pair.

solely to retrieve thermodynamic properties, essentially due to the uncertainty of the R(10,115) linestrength and its low absorbance level below 7000 K. The P(4,7) / P(1,25) line pair reaches its best sensitivity near 2000 K which is suitable for many combustion applications. The R(8,24) / P(1,25) line pair is more suited for higher temperature, 2000–9000 K, leveraging the large lower-state energy difference of R(8,24) and P(1,25), $\Delta E'' \approx 14,100$ cm^{-1}. This line pair is the key to extending the temperature range of this sensor. Therefore, using two-line area ratios from 2000 K to 8000 K, the 2010.6–2011.6 cm^{-1} region provides a temperature uncertainty better than 2% and a mole fraction uncertainty better than 6%. The best range for each line pair is leveraged and the sensitivity is improved by accounting for all of them in the Boltzmann-plot fitting procedure described in the next section.

2.2 Boltzmann population fit

In this work, instead of using a single line pair, we leveraged the rovibrational state population information provided by the four lines fitted in the 2010.6–2011.6 cm^{-1}, see Fig. 4. The linestrength of a single transition i is a function of temperature, T, the partition function $Q(T)$, the ground state energy of the transition E_i'', the wavenumber of the transition ν_i, and a reference temperature usually taken at $T_0 = 296$ K [31, 34].

$$S_i(T) = S_i(T_0) q(T, \nu_0) \exp\left[-\frac{hcE_i''}{k_B}\left(\frac{1}{T} - \frac{1}{T_0}\right)\right] \quad (7)$$

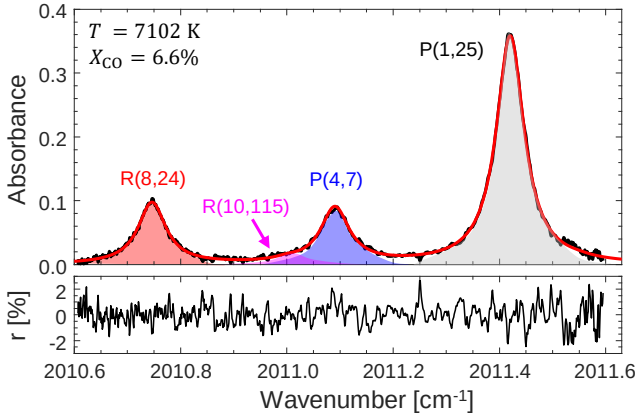

Fig. 4 Typical fit of the CO absorption spectrum between 2010.6 and 2011.6 cm^{-1}.

To shorten the mathematical expressions, the reference linestrength will be noted $S_i^0 = S_i(T_0)$. The term $q(T, \nu_0)$ accounts for partition function variation multiplied by a stimulated emission factor:

$$q(T, \nu_0) \approx q(T) = \frac{Q(T_0)}{Q(T)} \frac{1 - \exp\left(-\frac{hc}{k_B T}\nu_0\right)}{1 - \exp\left(-\frac{hc}{k_B T_0}\nu_0\right)} \quad (8)$$

We used the average wavenumber, $\nu_0 \approx 2011$ cm^{-1}, to calculate $q(T)$, which is a valid approximation[1] of the stimulated emission factor within 0.1%. The line-by-line spectral information, see Table 1, and the partition function are retrieved from the 2020 CO HITEMP database [35, 36]. Taking the natural logarithm of Eq. 7, we obtain:

$$\ln(S_i(T)) = \ln(S_i^0) + \ln(q(T)) - \frac{hc}{k_B} E_i \left(\frac{1}{T} - \frac{1}{T_0}\right) \quad (9)$$

Equation 2 can be combined into Eq. 9 to show the number density dependence:

$$\ln\left(\frac{A_i}{S_i^0}\right) = \ln(L n_{CO} q(T)) - \frac{hc}{k_B}\left(\frac{1}{T} - \frac{1}{T_0}\right) E_i \quad (10)$$

This linear relation is a direct representation of the Boltzmann distribution of CO internal states and it can be shown[2] that A_i/S_i^0 is related to the degree which the lower state of the transition i is populated (relative to the population at T_0).

[1] This approximation is valid for any lines that are spectrally close. For spectral separation higher than 1 cm^{-1}, the impact of this approximation would have to be recalculated.

[2] The line area is proportional to the linestrength, which is proportional to n_B'', the lower state population of transition i, i.e., $A_i \propto S_i(T) \propto n_B''$ [31, 34]. Thus, the term A_i/S_i^0 scales intuitively with the ratio of the transition ground state population at T and T_0:

$$A_i/S_i^0 \propto n_B''(T)/n_B''(T_0)$$

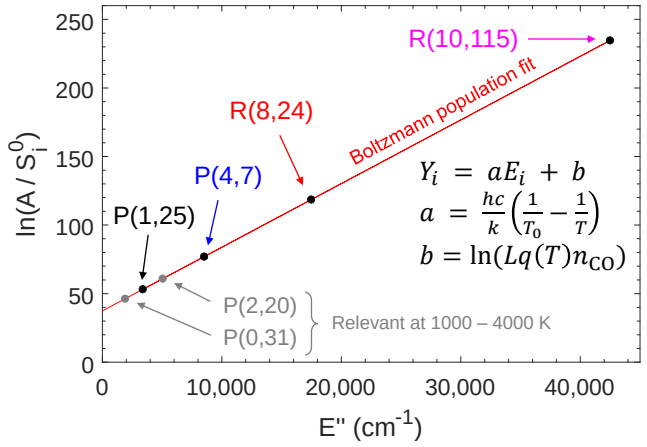

Fig. 5 Boltzmann plot of the four rovibrational states fitted in Fig. 4. Error bars are too small to be visible but are propagated during the linear fit following the method of York et al. [37].

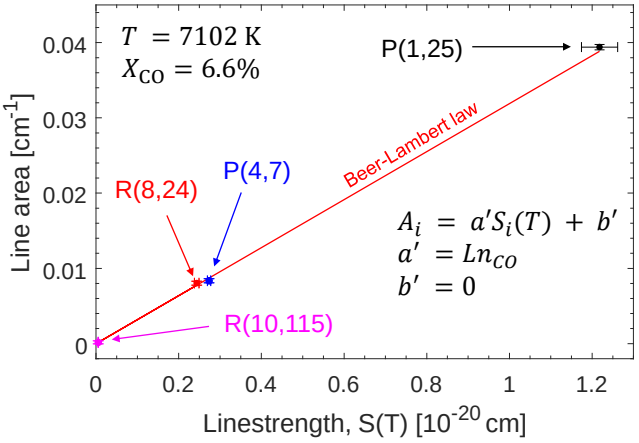

Fig. 6 Fit of the Beer-Lambert law accounting for error-bars across the four transitions fitted in Fig. 4.

Equation 10 has a linear form $Y = aE_i + b$ with

$$a = \frac{hc}{k_B}\left(\frac{1}{T_0} - \frac{1}{T}\right) \tag{11}$$

$$b = \ln(n_{CO} L q(T)) \tag{12}$$

An example of a Boltzmann distribution fit is given in Fig. 5. The temperature and number density can then be solved using:

$$T = \frac{1}{1/T_0 - a k_B/hc} \tag{13}$$

$$n_{CO} = \frac{\exp(b)}{Lq(T)} \tag{14}$$

The linear function coefficients, a and b, can be fitted accounting for uncertainty propagation [37] and, following the methods derived in the appendix (see Eq. 22), the temperature uncertainty is:

$$\frac{\delta T}{T} = \frac{k_B}{hc} T \delta a \tag{15}$$

The derivation of δn_{CO} from the differentiation of Eq. 14 is not as straightforward because the terms b and $q(T)$ are correlated. Therefore, with the knowledge of temperature determined in Eq. 13, the linestrength, $S(T)$ can now be calculated and used in the Beer-Lambert law repeated here for clarity:

$$A_i = n_{CO} L S_i(T) \tag{2}$$

Equation 2 presents the form $A_i = a'S_i + b'$. In the present fitting procedure, the intercept b' is not fixed to 0 and is used to verify the validity of the fit. Fitting Eq. 2 and accounting for uncertainty propagation [37], see Fig. 6, n_{CO} and δn_{CO} can be determined:

$$n_{CO} = \frac{a'}{L} \tag{16}$$

$$\frac{\delta n_{CO}}{n_{CO}} = \frac{\delta a'}{a'} + \frac{\delta L}{L} \tag{17}$$

Using either Eq. 14 or Eq. 16 provides the same number density. However, the uncertainty derivation is more straightforward from Eq. 16 and avoids dealing with correlated variables.

Therefore, in this work, Eqs. 13 and 15 are used for temperature measurements, whereas Eqs. 16 and 17 are used for number density. Assuming the same uncertainties employed previously for the the line pairs comparisons ($\delta S_i^0/S_i^0$, $\delta A_i/A_i$, and $\delta L/L = 1\%$), the uncertainty of the multi-line fit is calculated in Fig. 3. For $T \leq 2000$ K, the temperature and number density sensitivity is dominated by the P(4,7) / P(1,25) pair because the other transitions are too weak. In this case, the multi-line method is mathematically equivalent to the conventional two-line method and provides identical values and uncertainty. For $T \geq 2000$ K, the multi-line fit takes advantage of the P(4,7), P(1,25), and R(8,24) transitions and provides a lower uncertainty than any transition pair, whereas the R(10,115) transition improves the uncertainty for $T \geq 7000$ K. The sensitivity improvement is particularly visible in the number density uncertainty, which is below 4% across the 2000–8000 K range. To summarize, this multi-line fitting technique presents the advantage of leveraging all of the spectral information and provides: (1) A better uncertainty in temperature and number density than using a single line pair, see a comparison in Fig. 3. (2) A unique one-step post-processing technique across the entire range of temperature explored in this work.

It should be noted that rotational and vibrational temperatures could be measured independently given that at least three different vibrational levels can be probed in this spectrum. The rovibrational distribution is ideal given that the P(1,25)/R(8,24) line pair is mostly sensitive to vibrational temperature across seven vibrational levels, while the combination of the vibrational temperature and the P(1,25)/P(4,7) pair can be used to

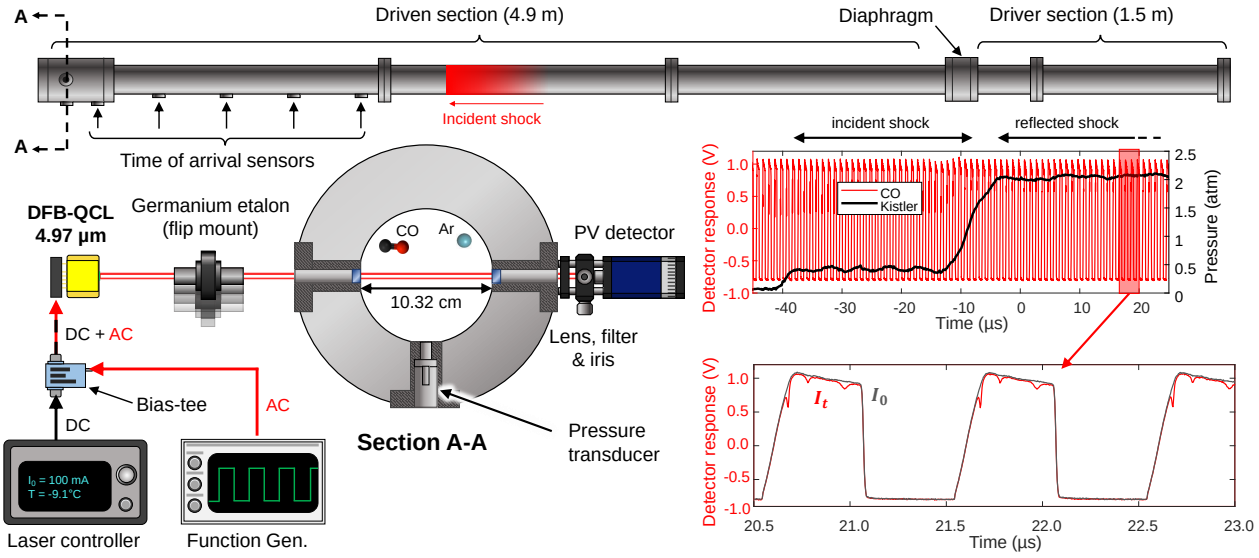

Fig. 7 (Left) Optical alignment setup mounted on the UCLA high-enthalpy shock tube (HEST). (Right) Sample raw detector and pressure measurements. In the inset, the time-resolved measurements (in red) are compared with the averaged background (in grey).

retrieve the rotational temperature. The opportunity to leverage the wide spacing in vibrational levels offered by this spectral range is however beyond the scope of this paper and left for future work.

2.3 Fitting procedure

In this section, the fitting procedure of each measurement is detailed. The entire 2010.6–2011.6 cm^{-1} spectrum is fitted by four Voigt functions, see Fig. 4. The area and broadening of these lines are varied until the sum of the squared difference (residual) between the experiment and the simulation reaches a minimum. A baseline is also fitted and subtracted from the experimental spectrum to account for potential background variations (beam steering, emission, laser fluctuation, etc.). Similar results are obtained with a constant or a linear baseline. The spectra are fitted using Voigt profiles which provided satisfactory noise-level residuals. During the fitting loop, a single Gaussian width is floated across the entire spectrum. The collisional broadening is floated independently for the four lines and, as a verification of the fit quality, is found to track the trend of the pressure variations measured by the shock-tube piezoelectric pressure sensor. As demonstrated in Fig. 4, the residual normalized by the peak absorbance is typically within 2%.

Once the areas of the four main transitions are retrieved, a Boltzmann population fit is performed using the algorithm of York et al. [37]. An example of a Boltzmann distribution fit is shown in Fig. 5, corresponding to a temperature T = 7102 K. In this figure, the energy difference of the current line selection can be readily compared to that of the previous line pair used for combustion sensing in the 2000–3000 K range [30]. The temperature is calculated using Eq. 13 and the temperature uncertainty is calculated using Eq. 15. Then, the Beer-Lambert law in Eq. 2 is fitted for the four measured areas to retrieve the CO number density, through Eq. 16, and the corresponding uncertainty, through Eq. 17. An example is shown in Fig. 6, where the Beer-Lambert law is fitted from the data of Fig. 4. In this particular case, the constant of the linear fit, b', is close to zero which indicates the accuracy of the measurement.

3 Experimental setup

Controlled experiments at high temperatures were performed to validate the aforementioned methods and demonstrate capability. Extreme temperatures are often generated in laboratory settings using plasma torches, arcjets, and shock tubes [3, 4, 38]. Among these devices, shock tubes can generate the highest temperatures across a range of pressure with high certainty in gas composition and thermodynamic state. Due to these advantages, shock tubes are well-suited for developing and validating a laser absorption sensor. In this study, the UCLA high-enthalpy shock tube (HEST), extensively described in previous works [39, 40] and presented in Fig. 7, is used to generate temperature and pressure conditions across 2000–12,000 K at 0.3–3 atm. Incident shock waves at speeds of 1.7–2.5 km/s are generated in gas mixtures of 5-20% CO:Ar. Helium is used as a driver gas. Before each shock, the driven section is turbo-vacuumed to less than 500 µTorr. The shock-wave time of arrival is measured by five piezoelectric sensors (Dynasen, CA-1135) located in the driven section. LAS measurements are conducted

2 cm from the shock-tube end wall through two 0.5-deg wedged sapphire windows. The reflected shock conditions are calculated using normal shock relations, assuming equilibrium conditions in the incident shock [41].

A stainless-steel mixing tank is used to prepare the gas mixtures manometrically. The tank is vacuumed down to less than 20 mTorr before preparing the mixtures. The purity of CO and Ar gases is certified above or equal to 99.99% by Airgas. The combined pressure and pure gas uncertainties result in a relative mixture composition uncertainty always below 0.05%. Thus, the uncertainty of the reference mixture is assumed to be negligible.

The optical setup is schematically presented in Fig. 7. The mean current and temperature of a quantum cascade laser (Alpes Lasers) is regulated using a laser controller (Arroyo 6310). A fixed (DC) current is sent to the laser via the controller, while a 1-MHz modulation is added to this DC component with a bias-tee circuit [20]. In this work, we modulated the laser with a trapezoidal waveform which presents a larger spectral scan-depth compared to sine or sawtooth modulations [30]. The current amplitude is set to 80% of the maximum allowed by the laser manufacturer. This setting represents a compromise between hardware safety and spectral scan-depth, reaching 1 cm^{-1}. The trapezoidal waveform, shown in Fig. 7, presents a ramp on the increasing side. This ramp prevents the temporal frequency content of the raw electrical signal from being higher than the limiting bandwidth of the detection system (200 MHz) when narrow absorption features are present in the scan. Following the recommendations of [30], we ensured that the equivalent time to scan an FWHM of the CO line is below 10 ns (twice 1/200 MHz).

The detection is performed by a photovoltaic (PV) detector (Vigo, PVI-4TE-5-1x1, 10 Hz–205 MHz bandwidth) whose output is sent to a Tektronix oscilloscope (MSO44 model, bandwidth 200 MHz) sampling the data at 6.25 GS/s on a 12-bit scale. The laser beam is focused on the detector chip using an AR-coated calcium-fluoride lens (20-mm focal length) and the broadband emission of the shock-heated plasma is attenuated by a narrow band-pass filter near 5 µm. The raw data acquired on the oscilloscope are presented in Fig. 7 and synchronized with the pressure measurement performed by a high-speed pressure transducer (Kistler, 601B1). An inset of Fig. 7 gives a comparison between the average background laser intensity recorded before the incident shock arrival, I_0, and the time-resolved transmitted laser intensity measured by the detector, I_t. The methods for conversion of I_0 and I_t into physical measurements were presented in the previous section. Validation and demonstration of sensor capabilities are presented in the following sections.

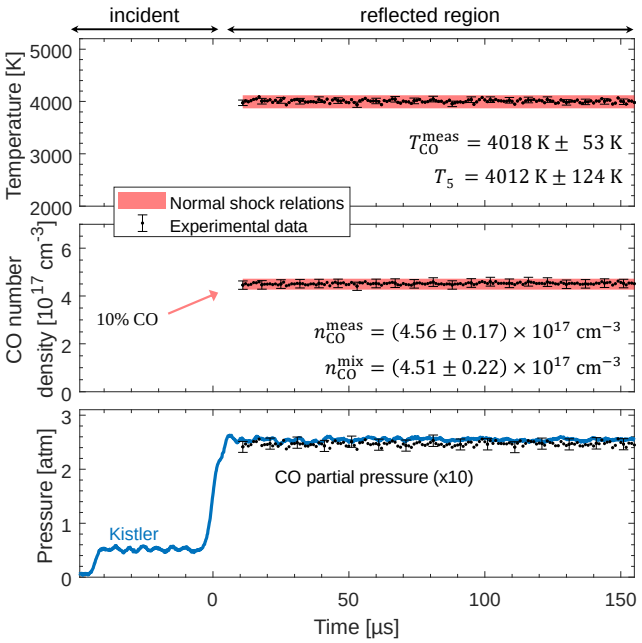

Fig. 8 Demonstration of the measurement accuracy and precision in a non-reacting case. The red swath represents the shock relation accuracy: 2% for the temperature (T_5) and 5% for the CO number density (from T_5 and p_5).

4 Sensor validation

In this section, a set of shock-tube measurements serve to validate the sensor presented in this work. The temperature and CO number density are compared to the values predicted by ideal reflected shock relations from 2300 to 8100 K. The simulation of an atmospheric gas at equilibrium shows that pure CO will be dissociated by more than 20% above 6000 K [2]. Thus, for a shock-heated gas below 6000 K, the timescale of CO kinetics (mainly dissociation) is long enough to be neglected during the test time (on the order of 100s of µs). For temperatures above 6000 K, only the first few microseconds after the reflected shock are used for the temperature validation. The negligible effect of CO dissociation is ensured by comparing the post-shock CO number density with its expected level.

As an initial demonstration of the sensor, the upper panel of Fig. 8 shows the measured temperature, T_{CO}^{meas}= 4018 ± 53 K, and the temperature calculated using normal shock relations, T_5 = 4012 ± 130 K . The uncertainties of the shock-heated gas thermodynamic properties are calculated by numerically evaluating a Taylor expansion of the normal shock relations (see Eq. 22 in Appendix A) [41]. The uncertainties on the initial driven section fill pressure (p_1), the driven mixture composition, and the initial temperature have a negligible impact on the T_5 and p_5 uncertainty, which are mostly dominated by the shock speed uncertainty (1360 ± 15 m/s in this example). In the computation of T_5, we assume that this incident shock region is vibrationally relaxed before the

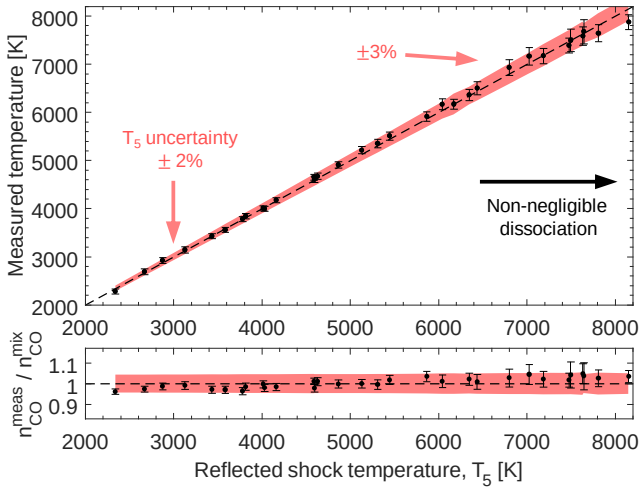

Fig. 9 Measured temperatures and CO mole fractions compared with those predicted by normal shock relations. The uncertainties of the normal-shock predictions are represented by a red swath.

arrival of the reflected shock. However, in the incident region, the areas of the probed transitions are sometimes not completely at steady state before the reflected shock, which indicates partial vibrational relaxation. Assuming a vibrationally frozen incident shock would slightly reduce T_5 by only 1-2% because the mixture is mainly composed of argon. Given that the incident shock is at least partially relaxed, this contribution to the uncertainty on T_5 is assumed to be at most 1%. The resulting uncertainty is near 3% for T_5, and 4% for p_5, which is representative of all the conditions explored in this work. In the present example of Fig. 8, $T_5 = 4012 \pm 124$ K which matches the value measured by LAS.

In the middle panel of Fig. 8, the measured number density of CO is also compared with the mixture composition. The CO number density in the reflected region is calculated based on the ideal gas law and the normal shock calculations:

$$n_{\mathrm{CO}}^{\mathrm{mix}} = X_{\mathrm{CO}} \frac{p_5}{k_{\mathrm{B}} T_5} \tag{18}$$

Therefore, as shown in Eq. 19, the p_5 and T_5 uncertainties propagate to the reference CO number density and give $n_{\mathrm{CO}}^{\mathrm{mix}} = (4.51 \pm 0.22) \times 10^{17} \mathrm{cm}^{-3}$.

$$\frac{\delta n_{\mathrm{CO}}^{\mathrm{mix}}}{n_{\mathrm{CO}}^{\mathrm{mix}}} = \sqrt{\left(\frac{\delta p_5}{p_5}\right)^2 + \left(\frac{\delta T_5}{T_5}\right)^2} \tag{19}$$

This value matches the measured number density, $n_{\mathrm{CO}}^{\mathrm{meas}} = (4.56 \pm 0.17) \times 10^{17} \mathrm{cm}^{-3}$, calculated using Eqs. 16 & 17. Details regarding the T_5 and p_5 uncertainty calculation are given in Appendix B

Similar measurements of T and n_{CO} are performed for temperatures ranging from 2300 to 8100 K and compared to T_5 and $n_{\mathrm{CO}}^{\mathrm{mix}}$. The results, summarized in Fig. 9, show that the measured temperatures and number densities match the values determined by normal shock relations within their uncertainties. From 2300 to 8100 K, the typical T_5 uncertainty increases from 2 to 3% and the CO number density uncertainty increases from 4 to 5 %. Further validation above 8100 K would be difficult to perform because the typical timescale of CO dissociation becomes comparable to 1 µs, the time resolution of this measurement. Quasi-steady-state conditions could be achieved with lower pressures (to slow the impact of dissociation) but would require a longer absorption pathlength (for improved SNR).

5 Sensor demonstrations

In this section, two time-resolved sensing demonstrations are performed to resolve thermochemical kinetics at high temperatures and the sensor performance is discussed.

5.1 CO dissociation above 8000 K

Above 8000 K, CO dissociation effects can be readily observed. The temperature and number density measured for a 10% CO:Ar mixture shock-heated near 9800 K are shown in Fig. 10. For an initial pressure at $p_5 =$ 2.09 atm, the CO number density drops and stabilizes after approximately 100 µs. At these conditions, the vibrational relaxation time is below 0.2 µs [42, 43]. In 100 µs, the temperature drops from 9000 K to 7000 K primarily due to the endothermic dissociation of CO. The partial pressure of CO ($p_{\mathrm{CO}} = n_{\mathrm{CO}} k_B T$) is compared to the pressure reading of the piezoelectric sensor (Kistler) in the lower panel of Fig. 10 to quantitatively indicate the dissociation of CO. To emphasize the effect of kinetic CO dissociation, p_{CO} is rescaled to account for the initial CO dilution. At the end of the test time, t = 200 µs, the mole fraction of CO has dropped from 10% to nearly 5%.

The measurements are compared to a 0-D kinetic simulation performed in Cantera [44] based on the high-temperature kinetic mechanisms of Johnston et al. [45] and Cruden et al. [18]. The kinetic mechanism of Cruden et al., optimized[3] for T above $\sim$ 6000 K, is employed as a baseline with the inclusion of the CO dissociation by Ar taken from Johnston et al.:

$$\mathrm{CO} + \mathrm{Ar} \longleftrightarrow \mathrm{C} + \mathrm{O} + \mathrm{Ar} \tag{R1}$$

A Cantera 0-D constant-pressure reactor simulates the shock-heated gas. The reactor pressure and temperature are updated in the simulation time loop according to an isentropic compression law to account for the

[3] In the work of Cruden et al., relaxation temperatures measured by OES behind incident shock waves in pure CO were utilized to select two reaction sets for incident shock waves in the 3.4–6.6 km/s range (T below $\sim$ 6000 K) and 6.6–9.5 km/s range (T above $\sim$ 6000 K).

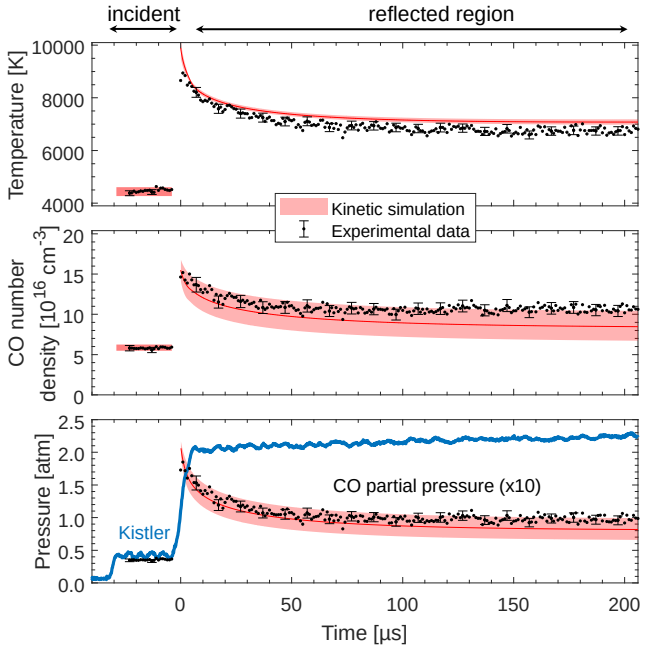

Fig. 10 Reacting case showing CO dissociation for T_5= 9892 K, $p_5 = 2.09$ atm, and $X_{CO} = 10\%$. The red swaths represent the uncertainty propagation of T_5 and p_5 in the 0-D kinetic modeling.

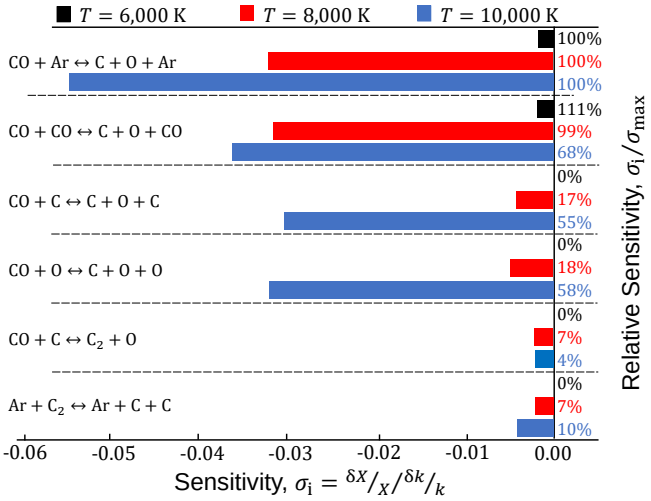

Fig. 11 Sensitivity of CO yield at $p_5 = 2$ atm for $T_5 = 6000$, 8000, and 10000 K in a 10% CO:Ar mixture. The relative sensitivity of each reaction compared to (R1) is shown on the right panel (in %).

slight pressure increase measured by the piezoelectric sensor (+1 mbar/100 µs). In Fig. 10, our measurements are compared to a CANTERA simulation performed at T_5 and p_5. Additional simulations are performed at the bounds of the combined T_5 and p_5 uncertainties and are represented by a red swath in Fig. 10. Note that the kinetic rate uncertainties are not included in this work. The numerical and experimental trends globally agree, with temperature and CO partial pressure dropping. For t $\geq$ 100 µs, the simulated temperature decreases slightly slower than the experimental ones, whereas the simulated CO partial pressure decreases faster than the experimental ones.

In the present work, sensitivity σ_i of reaction i is defined in Eq. 20 where $\delta X_{CO}/X_{CO}$ is the relative change of CO mole fraction for a given relative change in the reaction rate k_i, $\delta k_i/k_i$.

$$\sigma_i = \frac{\delta X_{CO}/X_{CO}}{\delta k_i/k_i} \tag{20}$$

In this case, the sensitivity is evaluated for $\delta k_i/k_i = 0.5$ and $\delta k_i/k_i = 2$. The average sensitivity of these two cases is presented in Fig. 11 to identify the main reactions at work. The sensitivities are calculated at $P = 2$ atm and $X_{CO} = 10\%$ and qualitatively represent the 0.3–3 atm range explored in this study. As could be predicted for a highly diluted CO mixture, CO dissociation is driven by CO-Ar collisions (R1). However, the reaction rate of CO-CO collisions (R2) is one order of magnitude higher than that of (R1) and also plays a key role in the dissociation kinetics.

$$CO + CO \longleftrightarrow C + O + CO \tag{R2}$$

The slight deviation between experimental and numerical results suggests that further tuning of these rates could be performed in future work using this sensor. Other reactions are less dominant until a temperature of 10,000 K is reached, which is treated in the next subsection.

5.2 CO dissociation above 9000 K

In a second example presented in Fig. 12, the normal shock relations predict reflected conditions near 12,000 K and 3 atm. At these extreme conditions, the vibrational relaxation time is shorter than 0.1 µs [42, 43]. The effect of the kinetic dissociation is directly visible in this plot with a significant decrease in temperature ($\Delta T = 4{,}000$ K), CO number density, and CO partial pressure in less than 50 µs. A fast initial temperature drop of 200 K/µs is recorded, which can be observed accurately with the MHz-rate capabilities presented in this work.

It can be noted that the transition between the incident and reflected shock regions takes approximately 4 µs. This effect is a direct result of a shock bifurcation, where an oblique shock propagates in the shock tube boundary layer and precedes the normal reflected shock in the bulk flow [46]. The boundary layer effect is typically more pronounced with increasing specific heat ratio and shock Mach numbers. The shock bifurcation induces a moderate beam steering effect (compared to the normal shock beam steering) but can be recorded [46]. Therefore, following the recommendations of Peterson and Hanson [46], we set the zero time using the laser

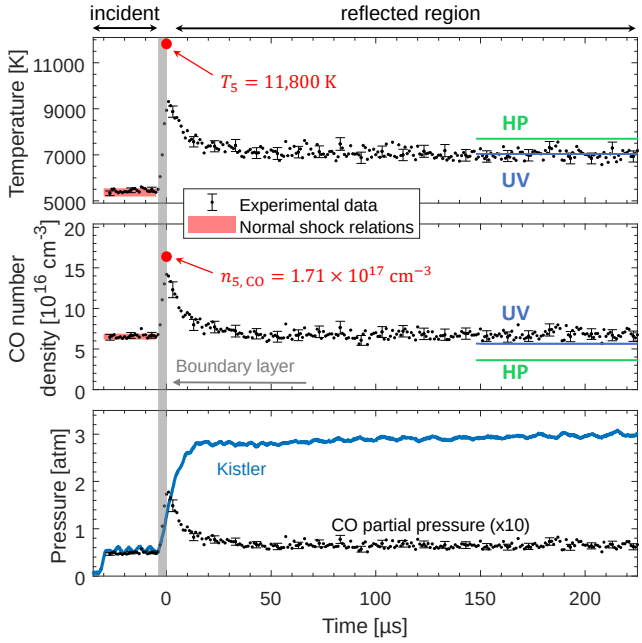

Fig. 12 Reacting case showing CO dissociation for T_5= 11,880 K, p_5 = 2.84 atm, and X_{CO} = 10%. The solid lines represent the equilibrium values for a constant HP reactor (blue) or constant UV reactor (green).

scan presenting the strongest beam steering. The period of moderate beam steering preceding the zero time lasts for 4 µs and corresponds to the temperature increase period reported in Fig. 12. The values reported in this short period are therefore due to shock bifurcation and averaged along the beampath. The measured temperatures are representative of the path-averaged temperature, see supporting validations in Appendix C.

As demonstrated in Fig 11, other reactions than (R1) and (R2) are non-negligible above 10,000 K. Other reaction, such as C and O ionization by electron impact also play a role in the CO dissociation. These reaction rates are highly sensitive to the electron temperature, which is supposed to be equilibrated to the translational temperature in Cantera. The electron temperature is however known to lag behind the translational temperature [47, 48], which complicates the kinetics beyond this paper's scope. Therefore, these measurements are compared to the equilibrium thermodynamic state calculated assuming constant enthalpy and pressure (HP) and constant internal energy and volume (UV), which are good approximations of the 0-D behavior of shock-heated mixtures [49]. The steady-state measurement is close to the UV case and deviates from the HP equilibrium. In this case, the UV approximation is better than the HP one. This could probably be due to the slight pressure increase in the reflected region (2% increase per 100-µs period).

Note that two temperatures of 9129 and 9310 K are reported in Fig 12, above the maximal tabulated temperature of the HITRAN partition function (9000 K). For these measurements, the partition function is linearly extrapolated, adding uncertainty to the number density of these two points. However, the temperature measurement is not dependent on the partition function. As such, despite the difficulties of validation, this sensor is suitable for temperatures well above 9000 K, near 1 eV.

6 Conclusions

A mid-infrared laser absorption sensor was developed for CO number density and temperature sensing at temperatures higher than 2000 K relevant for arc plasma, detonation combustion, and planetary entry applications. Using a DFB-QCL laser, the multi-line spectrum is scanned at 1 MHz using RF diplexing of the laser current injection and waveform tailoring. Novel line selection near 2011 cm^{-1} (4.97 µm) presents four distinct rovibrational transitions spectrally separated across ∼1 cm^{-1}. Compared to other line selections more adapted for low-pressure and airbreathing combustion environments, these transitions present improved temperature and number density sensitivity at these extreme temperatures, as supported by uncertainty analysis. The temperature and number density are determined by performing a fit of the rovibrational CO Boltzmann distribution across $\Delta E''_{\max}$ = 39,000 cm^{-1}. This method is a more versatile fitting procedure compared to using a single pair of lines adapted for a narrower range of temperature and provides lower measurement uncertainties. The mid-range of the sensor performance exhibits uncertainty of approximately 2% in temperature and 3-4% in species number density. In addition, the Boltzmann population fitting of the selected transitions is more robust to temperature non-uniformity. The precision and accuracy of the sensor are validated by shock tube measurements from 2300 to 8100 K. The sensor utility is demonstrated during CO dissociation at near-electron-volt temperatures relevant for high-speed planetary entry applications, matching a kinetic simulation and measuring temperatures up to 9310 K.

Acknowledgements

This work was sponsored by the NASA's Space Technology Research Grants Program (N. Minesi and M. Richmond, award 80NSSC21K0066). Supplementary support was provided by a NASA Space Technology Research Fellowship (C. Jelloian, grant 80NSSC18K1158), the U.S. National Science Foundation (N. Kuenning, award 1752516), and the Air Force Research Laboratory (A. Nair, award FA9300-19-P-1503).

A Uncertainty analysis

In this section, we derive the uncertainty in the temperature and number density measurements with respect to the spectroscopic parameters of a given line pair and the experimental noise. The uncertainty analysis follows and expands the work presented in [20]. The uncertainty of f, function of x_i variables, can be calculated using a Taylor expansion:

$$df(x_1, x_2, \cdots) = \frac{\partial f}{\partial x_1} dx_1 + \frac{\partial f}{\partial x_2} dx_2 + \cdots \tag{21}$$

Assuming the measured variables, x_i, are independent of one another, and that the errors in the measured variables, δx_i, are independent of one another [50], we get the uncertainty of f, δf, as a function of its partial derivatives:

$$(\delta f)^2 = \left(\frac{\partial f}{\partial x_1}\delta x_1\right)^2 + \left(\frac{\partial f}{\partial x_2}\delta x_2\right)^2 + \cdots \tag{22}$$

In the following sections, the relations of temperature with the linestrengths and areas of a line pair are derived and Eq. 22 is applied.

A.1 Temperature uncertainty

The temperature uncertainty for a line pair is derived from Eqs. 7 and 8, which are repeated here for clarity. The linestrength of a single line i is a function of temperature, T, the partition function $Q(T)$, the ground state energy of the transition E_i'', the wavenumber of the transition ν_i, the Boltzmann constant k_B, and $T_0 = 296$ K [31, 34].

$$S_i(T) = S_i(T_0) q(T, \nu_0) \exp\left[-\frac{hcE_i''}{k_B}\left(\frac{1}{T} - \frac{1}{T_0}\right)\right] \tag{7}$$

The term $q(T, \nu_0)$ accounts for partition function variation multiplied by a stimulated emission factor:

$$q(T, \nu_0) \approx q(T) = \frac{Q(T_0)}{Q(T)} \frac{1 - \exp\left(-\frac{hc}{k_B T}\nu_0\right)}{1 - \exp\left(-\frac{hc}{k_B T_0}\nu_0\right)} \tag{8}$$

The ratio of two linestrengths, R, is equal to the ratio of the integrated absorbance of two lines A and B, A_A and A_B:

$$R(T) = \frac{S_\mathrm{A}(T)}{S_\mathrm{B}(T)} = \frac{A_\mathrm{A}}{A_\mathrm{B}} \tag{3}$$

The $q(T)$ terms cancel out in Eq. 3 because ν_0 variation has a weak impact on $q(T)$ for two neighboring lines and the function $R(T)$ can be expressed as:

$$R(T) = \frac{S_\mathrm{A}^0}{S_\mathrm{B}^0} \exp\left[-\frac{hc}{k_\mathrm{B}}(E_\mathrm{A}'' - E_\mathrm{B}'')\left(\frac{1}{T} - \frac{1}{T_0}\right)\right] \tag{23}$$

Differentiating Eq. 3, using Eq. 23, and setting $\Delta E = E_A'' - E_B''$, we get:

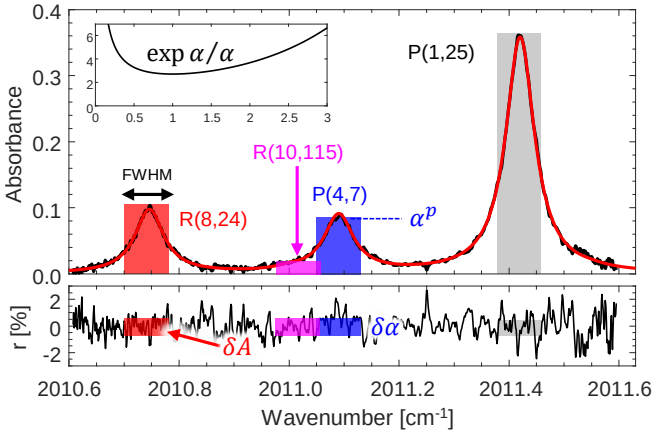

Fig. 13 Illustration of the uncertainty analysis performed assuming simplified areas, $A = \alpha^p \Delta\nu$, and area uncertainties $\delta A = \delta\alpha\Delta\nu$. The inset shows the uncertainty optimum reached for $\alpha = 1$, the minimum of $\exp(\alpha)/\alpha$.

$$\left(\frac{dR}{R} =\right) \frac{dS_A^0}{S_A^0} - \frac{dS_B^0}{S_B^0} + \frac{hc}{k_B}\frac{\Delta E}{T^2} dT = \frac{dA_A}{A_A} - \frac{dA_B}{A_B} \tag{24}$$

which can be written:

$$\frac{dT}{T} = \frac{k_B}{hc}\frac{T}{\Delta E}\left(-\frac{dA_A}{A_A} + \frac{dA_B}{A_B} + \frac{dS_A^0}{S_A^0} - \frac{dS_B^0}{S_B^0}\right) \tag{25}$$

From here, the terms $\partial A_i/\partial T$, $\partial S_i^0/\partial T$ can be identified and, substituting Eq. 24 into Eq. 22 with T as f, the temperature uncertainty is obtained in Eq. 26:

$$\frac{\delta T}{T} = \frac{k_B}{hc}\frac{T}{\Delta E}\sqrt{\sum_{i=1}^{2}\left[\left(\frac{\delta S_i^0}{S_i^0}\right)^2 + \left(\frac{\delta A_i}{A_i}\right)^2\right]} \tag{26}$$

In this derivation, we neglected the contribution of the energy level uncertainty, $\delta E''$, which is close to the line position uncertainty and found to be $\delta E''/E'' \leq 10^{-6}$.

The area uncertainty, δA_i, is now related to the peak absorbance, α^{pk}. The area of the line can be approximated by the peak absorbance multiplied by the FWHM, i.e. $A_i \approx \alpha_i^{\mathrm{pk}} \Delta\nu$. The line area uncertainty can be estimated by a rectangle of height $\delta\alpha$, the absorbance noise, and width $\Delta\nu$, the FWHM of the line, i.e., $\delta A \approx \delta\alpha\Delta\nu$. An illustration of the absorbance area and area uncertainty is provided in Fig. 13.

$$\frac{\delta A_i}{A_i} \approx \frac{\delta\alpha\Delta\nu}{\alpha_i^{\mathrm{pk}}\Delta\nu} = \frac{\delta\alpha}{\alpha_i^{\mathrm{pk}}} \tag{27}$$

The absorbance is related to the measured amplitude of the non-absorbed laser intensity, I_0, and the transmitted intensity, I_t, see Eq.1:

$$\alpha(\nu) = -\ln\left(\frac{I_\mathrm{t}}{I_0}\right)_\nu \tag{1}$$

Differentiating Eq.1 we obtain:

$$d\alpha = -\frac{dI_\mathrm{t}}{I_\mathrm{t}} + \frac{dI_0}{I_0} \tag{28}$$

By using Eq. , with α as f, the absorbance noise $\delta\alpha$ can be related to the noise in the transmitted intensity, dI_t, and the noise in the background intensity, dI_0:

$$(\delta\alpha)^2 = \left(\frac{\delta I_\mathrm{t}}{I_\mathrm{t}}\right)^2 + \left(\frac{\delta I_0}{I_0}\right)^2 \tag{29}$$

The transmitted intensity noise, δI_t, is the root mean square of the oscilloscope voltage and hence includes the effective sum of the laser fluctuations, the detector noise and the oscilloscope noise. Unlike the analysis of Ref. [51], in this work, the noise of the background intensity is greatly reduced via signal averaging, such that $\delta I_0 \ll \delta I_\mathrm{t}$, which means that Eq. 29 simplifies to:

$$\delta\alpha = \frac{\delta I_\mathrm{t}}{I_\mathrm{t}} \tag{30}$$

This expression can be divided by α to find the relative noise in the absorbance measurement:

$$\frac{\delta\alpha}{\alpha} = \frac{1}{\alpha}\frac{\delta I_\mathrm{t}}{I_\mathrm{t}} = \frac{1}{\alpha}\frac{\delta I_\mathrm{t}}{I_0 \exp(-\alpha)} \tag{31}$$

The signal-to-noise ratio of the raw laser intensity is defined as $\mathrm{SNR} = I_0/\delta I_t$ and hence:

$$\frac{\delta\alpha}{\alpha} = \frac{1}{\mathrm{SNR}}\frac{\exp(\alpha)}{\alpha} \tag{32}$$

Equation 32 indicates the level of noise to be expected in an absorption measurement. When α^p is substituted for α in the denominator of both sides of the equation, the expected normalized residual r can be predicted for an absorbance measurement. This expression is approximately equal to the uncertainty in the area measurement, as indicated by Eq. 27. The ratio $\exp(\alpha)/\alpha$ indicates how much the relative noise in the raw intensity (1/SNR) is amplified to obtain the relative absorbance noise. As shown in the inset of Fig. 13, this function is minimized at $\alpha = 1$ at a value of e, indicating that at best, the absorbance noise is approximately 2.72 times the noise in the raw signal. When α is low, representing the optically-thin limit, the numerator is approximately 1, and the absorbance noise is inversely proportional to the absorbance. When α is high, the numerator dominates and the absorbance noise grows non-linearly with α, representing the optically-thick limit where I_t is close to 0 and below the noise level.

As indicated above, to approximate the uncertainty in an area measurement, the α in the denominator of Eq. 31 should be replaced by α_i^pk. The numerator is still a function of α, which is maximized at the peak absorbance, where the transmitted laser intensity is the lowest. To provide a conservative estimate of the area uncertainty, this peak absorbance noise is also used for the numerator, such that:

$$\frac{\delta A_i}{A_i} \approx \frac{1}{\mathrm{SNR}}\frac{\exp\left(\alpha_i^\mathrm{pk}\right)}{\alpha_i^\mathrm{pk}} \tag{33}$$

The substitution of Eq. 33 in Eq. 26 gives the relative uncertainty in T for a given line pair given in Eq. 4.

$$\frac{\delta T}{T} = \frac{k_B}{hc}\frac{T}{\Delta E}\sqrt{\sum_{i=1}^{2}\left[\left(\frac{\delta S_i^0}{S_i^0}\right)^2 + \left(\frac{1}{\mathrm{SNR}}\frac{\exp\left(\alpha_i^\mathrm{pk}\right)}{\alpha_i^\mathrm{pk}}\right)^2\right]} \tag{4}$$

A.2 Number density uncertainty

Substituting Eq. 5 to Eq. 22, we get:

$$\frac{\delta n_\mathrm{CO}}{n_\mathrm{CO}} = \sqrt{\left(\frac{\delta A_i}{A_i}\right)^2 + \left(\frac{\delta L}{L}\right)^2 + \left(\frac{\delta S_i}{S_i}\right)^2} \tag{34}$$

The uncertainty in the linestrength due to the temperature uncertainty must be separated from the reference linestrength uncertainty. The variation in the linestrength S is convoluted with the variation of the partition function, see Eq. 7, and its derivation is not straightforward to generalize to any molecule. In this work, we numerically evaluate the linestrength derivative with T and deduce:

$$\left(\frac{\delta S_i}{S_i}\right)^2 = \left(\frac{1}{S_i(T)}\frac{\partial S_i}{\partial T}\delta T\right)^2 + \left(\frac{\delta S_i^0}{S_i^0}\right)^2 \tag{35}$$

We obtain the number density uncertainty as:

$$\left(\frac{\delta n_\mathrm{CO}}{n_\mathrm{CO}}\right)^2 = \left(\frac{1}{\mathrm{SNR}}\frac{\exp\left(\alpha_i^\mathrm{pk}\right)}{\alpha_i^\mathrm{pk}}\right)^2 + \left(\frac{\delta L}{L}\right)^2 + \left(\frac{1}{S_i(T)}\frac{\partial S_i}{\partial T}\delta T\right)^2 + \left(\frac{\delta S_i^0}{S_i^0}\right)^2 \tag{6}$$

In this work, the pathlength is known within $\delta L/L = 1\%$. The uncertainty $\delta n/n$ is calculated in Fig. 3 using three line pairs available in the 2010.6 - 2011.6 cm^{-1} region. To minimize the overall uncertainty, the area from P(1,25) transition is taken because its peak absorbance is typically the closest to 1. This line also offers the lowest uncertainty in the reference linestrength, $\delta S^0_{P(1,25)} = 1$–2 %. Note that in the experimental results presented in this work, the uncertainty of the Boltzmann population fit are employed. The line pair uncertainties presented in Fig. 3 are only used to illustrate relative measurement accuracy of the different line pair combinations leveraged by the Boltzmann population fit method across the temperature range.

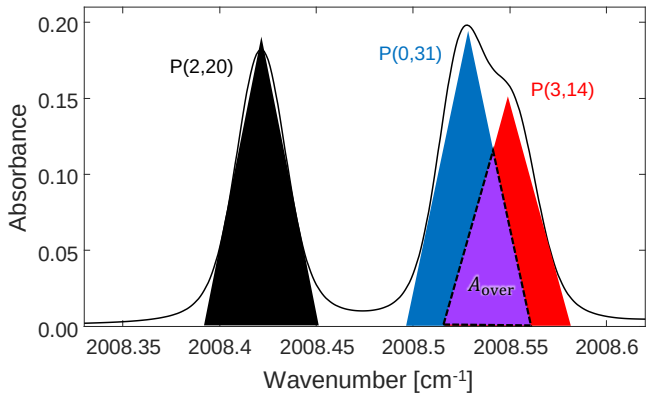

Fig. 14 Full CO spectrum calculated at $T = 8000$ K, $p = 1$ atm, and $X_{CO} = 10\%$ based on HITEMP database. The lineshapes are assumed to be triangles to calculate A_{over}, the overlap area of the P(3,14) and P(0,31) and ultimately estimate the error in fitting these lines.

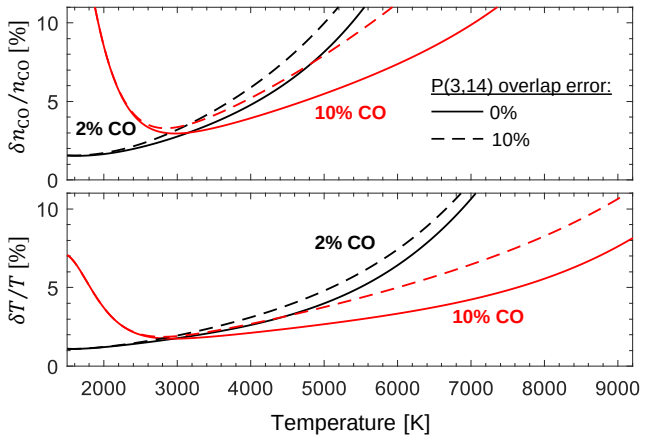

Fig. 15 δT and δn_{CO} calculated assuming the P(3,14) line area overlap, A_{over}, is perfectly taken into account, full line, and if 10% of A_{over} is erroneously attributed to the P(0,31) line, dashed line. The effect is calculated for 2% and 10% CO mixtures at 1 atm and $L = 10$ cm.

A.3 Non-isolated lines: perturbations due to neighboring features

The line selection used in this work presents large ΔE which improves the temperature uncertainty but also offers four spectrally separated lines. This is not the case for the line selection at 2008 cm^{-1} used in previous work, where the P(3,14) line overlaps with the P(0,31) line. This effect is evident above 3500 K, see Fig. 15, when the P(3,14) line has a peak absorbance similar to P(0,31). The contribution of the P(3,14) line can be subtracted using iterative Voigt fitting but it is difficult to estimate how the uncertainty of this correction propagates to the temperature and number density measurements [20, 29]. In this subsection, we numerically calculate the impact of the uncertainty generated by the subtraction of a neighboring line, taking as an example the line selection at 2008 cm^{-1}. The lineshape is assumed to be triangular to simplify the calculations, with the FWHM of the triangle set equal to that of the actual Voigt lineshape. A representation of this approximation is shown in Fig. 14. The overlapping area of the two lines, A_{over} in Fig. 14, can be calculated mathematically given the line peak absorbance, FWHM, and positions. When accounting for the P(3,14) line, the main source of uncertainty is estimated to arise from an erroneous allocation of the overlapping area to either P(0,31) and P(3,14). Assuming that 10% of A_{over} is wrongly attributed to P(0,31), another contribution to $\delta A_i/A_i$ in Eq. 26 and Eq. 34 leads to an increase of δT and δn. For a 2-% CO mole fraction adequate for measurements in combustion environments, Fig. 15 shows that, at 2000 K, a 10% error in the allocation of A_{over} leads to a negligible increase in temperature and number density uncertainty, 0.01% and 0.05%, respectively. This confirms that the uncertainty arising due to the P(3,14) line was negligible in previous work [20, 29]. However, at temperatures higher than 3500 K and 10% CO mole fraction, the temperature and number density uncertainty increase by several percents, which further motivates the use of the new line selection at those temperatures.

B Uncertainties in the reflected shock conditions

The method to calculate the uncertainty on p_5 and T_5 is given in this appendix. As described earlier, the reflected shock conditions are calculated using normal shock relations processed through a MATLAB code [41]. The normal shock relations require the knowledge of (1) p_1, the fill pressure, (2) T_1, the initial temperature, (3) x_i, the composition of the shock-heated gas, and (4) v_{end}, the speed of the shock on the endwall. The uncertainty of these parameters is propagated to the calculated T_5 and p_5 through a Taylor expansion method, see Eq. 22. The fill pressure uncertainty is assumed to be equal to the last digit of the most precise manometer that can be employed during the fill procedure, i.e. $\delta p_1 = 0.1$, 0.01 or 0.001 Torr. The temperature uncertainty is assumed to be $\delta T_1 = 1$ K. The mixture is prepared by subsequent filling of CO and Ar at increasing pressure. The species mole fraction uncertainty is calculated by accounting for the manometer precision in this step-by-step procedure and is negligible in this work, i.e. $\delta x_i/x_i \leq 0.05\%$. The shock position is determined through the reading of pressure transducers along the shock tube. The shock speed uncertainty is calculated by propagating the uncertainty in the shock position versus time through a York linear fit [37] accounting for the uncertainty in the pressure sensing positions ($\delta x = 1/16$ in.) and the time of arrival at each sensor (near 1 µs). In the speed range of this work, these two parameters contribute within the same order of magnitude to the speed uncertainty. As illustrated in Fig. 16, the resulting uncertainty on the speed is typically 10-30 m/s for shock speeds of 2000

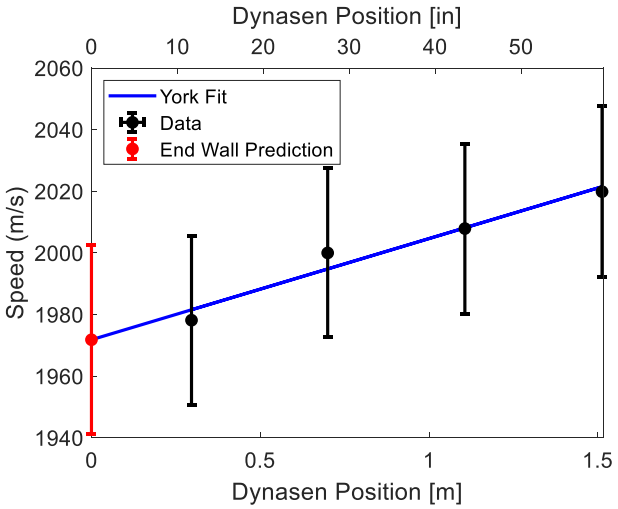

Fig. 16 Shock speed measured using five pressure transducers. The end-wall speed is calculated using the linear York fit of the data [37].

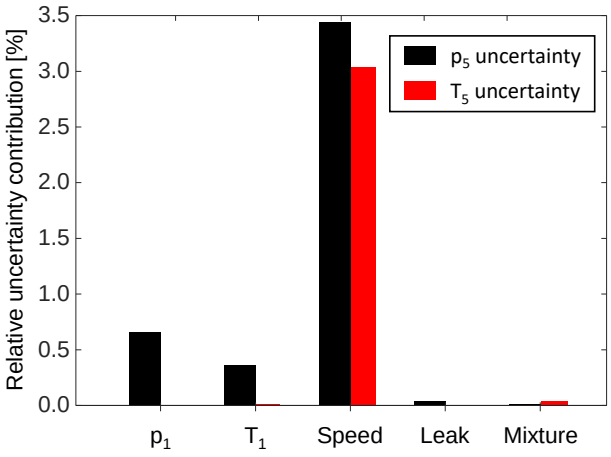

Fig. 17 Contributions to the p_5 and T_5 uncertainties.

m/s ($\leq 1.5\%$). We also included the uncertainty due to the shock tube leak rate in the calculation, by adding air to the mixture. The air leaked in the shock tube represents less than 0.5% of the mixture for the lowest p_1 of this study.

For the shock used as illustration in Fig. 16, the reflected shock heated conditions are $T_5 = 8013$ K ($\pm$ 3.1%) and $p_5 = 0.53$ atm ($\pm$ 4.5%). The contribution from each of the aforementioned sources to the total uncertainty in pressure and temperature is illustrated in Fig. 16. The uncertainties on p_1 and T_1 have a minor contribution to the total uncertainty and would be challenging to improve further. The shock speed measurement dominates the overall uncertainty. It can also be noted that the mixture uncertainty and the leak rate have negligible impact on p_5 and T_5, which indicates that our experimental procedure is adequate.

C Non-uniform path-integrated measurements

In this section, the robustness of this line selection to non-uniform temperature distribution is assessed. Let's define $\overline{S(T)}$ and $\overline{T}$ as the path-averaged linestrength and temperature weighted by the number density of the absorbing species, $n_{\mathrm{CO}}(l)$, that varies with the position along the beampath l [20, 52]:

$$\overline{S(T)} = \frac{\int_0^L n_{\mathrm{CO}}(l) S(T(l)) dl}{\int_0^L n_{\mathrm{CO}}(l) dl} \tag{36}$$

$$\overline{T} = \frac{\int_0^L n(l) T(l) dl}{\int_0^L n(l) dl} \tag{37}$$

Assuming a linear gradient of 1000 K across a constant pressure slab in Fig. 18, the linestrength deviation $\Delta S = \overline{S(T)} - S(\overline{T})$ is below 2% of $\overline{S(T)}$ for the three primary lines in the spectrum. This result indicates that the linestrength variation in temperature is close to linear using these lines. Hence, the temperature measurements should be close to the CO number density-weighted path-averaged temperature. This is verified by calculating ΔT defined in Eqs. 38, where R^{-1} is the inverse function of R defined in Eq. 3 and relating the ratio of linestrengths to temperature:

$$\Delta T = R^{-1}(\overline{S(T)}) - R^{-1}(S(\overline{T})) \tag{38}$$

The results, shown in Fig. 18, indicate that $\Delta T/\overline{T}$ is within 1% using the ratio of R(10,115), R(8,24), and P(4,7) with P(1,25) and assuming a uniform 1000-K gradient. Performing this calculation with a Boltzmann population fit, (in green in Fig. 18), the difference drops below 0.2%. An extreme-case estimate with a 3000-K gradient is calculated using a Boltzmann population fit and shows a maximum error of 4% compared to the average temperature. In conclusions, the Boltzmann fit of the four lines in the present wavenumber range is more robust to the bias induced by temperature gradients than the individual pair of lines taken separately. This robustness is essentially due to the R(10,115) transition, which positively bias non-uniform temperature measurements and compensates for the negatively bias temperature measurements induced by the other transitions. Therefore, the values reported in Fig. 12 during the 4-µs window displaying the propagation of the oblique shock are representative of the path-average temperature and CO number density and can be used for future studies of the oblique shock layer.

References

1. Glassman I, Yetter RA (2008) Combustion, vol 136, ed. 4 edn. Elsevier

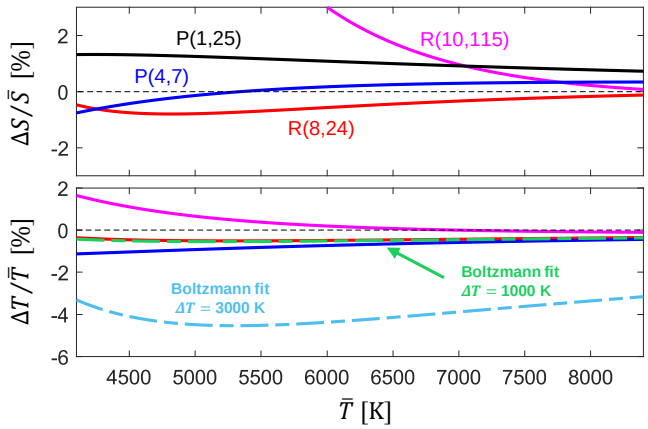

Fig. 18 (Top) Relative difference between $\overline{S(T)}$ and $S(\overline{T})$ assuming a linear gradient of 1000 K across an absorption slab. **(Bottom)** Relative error in temperature determination after fitting the integrated linestrength using the ratio of R(10,115), R(8,24), and P(4,7) with P(1,25), colored full lines. Two Boltzmann distribution fits have been performed at 1000 K (green dashed) and 3000 K (grey dashed).

2. Gordon S, McBride BJ, Gordon S, McBride BJ (1996) Computer Program for Calculation of Complex Chemical Equilibrium Compositions and Applications. January, NASA
3. Venkatramani N (2002) Industrial plasma torches and applications. Current Science 83(3):254–262, DOI 10.2307/24106883, URL https://www.jstor.org/stable/24106883
4. Nations M, Chang LS, Jeffries JB, Hanson RK, MacDonald ME, Nawaz A, Taunk JS, Gökçen T, Raiche G (2017) Characterization of a Large-Scale Arcjet Facility Using Tunable Diode Laser Absorption Spectroscopy. AIAA Journal 55(11):3757–3766, DOI 10.2514/1.J056011, URL https://arc.aiaa.org/doi/10.2514/1.J056011
5. Arora N, Sharma NN (2014) Arc discharge synthesis of carbon nanotubes: Comprehensive review. Diamond and Related Materials 50:135–150, DOI 10.1016/j.diamond.2014.10.001, URL http://dx.doi.org/10.1016/j.diamond.2014.10.001
6. Su Y, Yang Z, Wei H, Kong ESW, Zhang Y (2011) Synthesis of single-walled carbon nanotubes with selective diameter distributions using DC arc discharge under CO mixed atmosphere. Applied Surface Science 257(7):3123–3127, DOI 10.1016/j.apsusc.2010.10.127, URL http://dx.doi.org/10.1016/j.apsusc.2010.10.127https://linkinghub.elsevier.com/retrieve/pii/S0169433210014935
7. Maly R, Vogel M (1979) Initiation and propagation of flame fronts in lean CH4-air mixtures by the three modes of the ignition spark. Symposium (International) on Combustion 17(1):821–831, DOI 10.1016/S0082-0784(79)80079-X, URL http://www.sciencedirect.com/science/article/pii/S008207847980079X
8. Albrecht H, Bloss WH, Herden WH, Maly R, Saggau B, Wagner E (1977) New Aspects on Spark Ignition. SAE Technical Papers p 770853, DOI 10.4271/770853, URL https://doi.org/10.4271/770853
9. Pietanza LD, Guaitella O, Aquilanti V, Armenise I, Bogaerts A, Capitelli M, Colonna G, Guerra V, Engeln R, Kustova E, Lombardi A, Palazzetti F, Silva T (2021) Advances in non-equilibrium CO2 plasma kinetics: a theoretical and experimental review. The European Physical Journal D 75(9):237, DOI 10.1140/epjd/s10053-021-00226-0, URL https://doi.org/10.1140/epjd/s10053-021-00226-0https://link.springer.com/10.1140/epjd/s10053-021-00226-0
10. Maillard J, Pannier E, Laux CO (2022) Time-resolved Optical Emission Spectroscopy measurements of electron density and temperature in CO2 Nanosecond Repetitively Pulsed discharges. In: AIAA SCITECH 2022 Forum, American Institute of Aeronautics and Astronautics, Reston, Virginia, DOI 10.2514/6.2022-2368, URL https://arc.aiaa.org/doi/10.2514/6.2022-2368
11. Ceppelli M, Salden TPW, Martini LM, Dilecce G, Tosi P (2021) Time-resolved optical emission spectroscopy in CO 2 nanosecond pulsed discharges. Plasma Sources Science and Technology 30(11):115010, DOI 10.1088/1361-6595/ac2411, URL https://iopscience.iop.org/article/10.1088/1361-6595/ac2411
12. Minesi N, Stepanyan S, Mariotto P, Stancu GD, Laux CO (2020) Fully ionized nanosecond discharges in air: the thermal spark. Plasma Sources Science and Technology 29:85003, DOI 10.1088/1361-6595/ab94d3, URL https://doi.org/10.1088/1361-6595/ab94d3
13. Braun RD, Powell RW, Hartung LC (1990) Effect of Interplanetary Trajectory Options on a Manned Mars Aerobrake Configuration. NASA Technical Paper 3019
14. Cruden BA, Prabhu D, Martinez R (2012) Absolute Radiation Measurement in Venus and Mars Entry Conditions. Journal of Spacecraft and Rockets 49(6):1069–1079, DOI 10.2514/1.A32204
15. McGuire SD, Tibère-Inglesse AC, Laux CO (2016) Infrared spectroscopic measurements of carbon monoxide within a high temperature ablative boundary layer. Journal of Physics D: Applied Physics 49(48), DOI 10.1088/0022-3727/49/48/485502
16. Lewis SW, James CM, Morgan RG, McIntyre TJ, Alba CR, Greendyke RB (2017) Carbon ablative shock-layer radiation with high surface temperatures. Journal of Thermophysics and Heat Transfer 31(1):193–204, DOI 10.2514/1.T4902
17. Packan D, Laux CO, Gessman RJ, Pierrot L, Kruger CH (2003) Measurement and Modeling of OH, NO, and CO Infrared Radiation at 3400 K. Journal of Thermophysics and Heat Transfer 17(4):450–456, DOI 10.2514/2.6803, URL https://arc.aiaa.org/doi/10.2514/2.6803
18. Cruden BA, Brandis AM, Macdonald ME (2018) Characterization of CO thermochemistry in incident shockwaves. 2018 Joint Thermophysics and Heat Transfer Conference pp 1–22, DOI 10.2514/6.2018-3768
19. Lin X, Chen LZ, Li JP, Li F, Yu XL (2018) Experimental and Numerical Study of Carbon-Dioxide Dissociation for Mars Atmospheric Entry. Journal of Thermophysics and Heat Transfer 32(2):503–513, DOI 10.2514/1.T5152, URL https://arc.aiaa.org/doi/10.2514/1.T5152
20. Nair AP, Lee DD, Pineda DI, Kriesel J, Hargus WA, Bennewitz JW, Danczyk SA, Spearrin RM (2020) MHz laser absorption spectroscopy via diplexed RF modulation for pressure, temperature, and species in rotating

detonation rocket flows. Applied Physics B 126(8):138, DOI 10.1007/s00340-020-07483-8, URL https://link.springer.com/10.1007/s00340-020-07483-8

21. Vanderover J, Oehlschlaeger MA (2010) A mid-infrared scanned-wavelength laser absorption sensor for carbon monoxide and temperature measurements from 900 to 4000 K. Applied Physics B 99(1-2):353–362, DOI 10.1007/s00340-009-3849-5, URL http://link.springer.com/10.1007/s00340-009-3849-5
22. Bendana FA, Lee DD, Wei C, Pineda DI, Spearrin RM (2019) Line mixing and broadening in the v(1→3) first overtone bandhead of carbon monoxide at high temperatures and high pressures. Journal of Quantitative Spectroscopy and Radiative Transfer 239:106636, DOI 10.1016/j.jqsrt.2019.106636, URL https://linkinghub.elsevier.com/retrieve/pii/S0022407319304042
23. MacDonald ME, Cruden BA (2016) A tunable laser absorption diagnostic for measurements of CO in shock-heated gases. 46th AIAA Thermophysics Conference (June):1–12, DOI 10.2514/6.2016-3694
24. Macdonald ME, Brandis AM, Cruden BA (2017) Post-Shock temperature and CO Number density measurements in CO and CO2. 47th AIAA Thermophysics Conference, 2017 (June):1–18, DOI 10.2514/6.2017-4342
25. MacDonald ME, Brandis AM, Cruden BA (2018) Temperature and CO Number Density Measurements in Shocked CO and CO2 via Tunable Diode Laser Absorption Spectroscopy. In: 2018 Joint Thermophysics and Heat Transfer Conference, American Institute of Aeronautics and Astronautics, Reston, Virginia, pp 1–23, DOI 10.2514/6.2018-4067, URL https://arc.aiaa.org/doi/10.2514/6.2018-4067
26. Nair AP, Jelloian C, Morrow DS, Bendana FA, Pineda DI, Spearrin RM (2020) MHz mid-infrared laser absorption sensor for carbon monoxide and temperature behind detonation waves. In: AIAA Scitech 2020 Forum, American Institute of Aeronautics and Astronautics, Reston, Virginia, DOI 10.2514/6.2020-0733, URL https://arc.aiaa.org/doi/10.2514/6.2020-0733
27. Ruesch MD, Gilvey JJ, Goldenstein CS, Daniel KA, Downing CR, Lynch KP, Wagner JL (2022) Mid-Infrared Laser-Absorption-Spectroscopy Measurements of Temperature, Pressure, and NO X2 $\Pi 1/2$ at 500 kHz in Shock-Heated Air. AIAA Science and Technology Forum and Exposition, AIAA SciTech Forum 2022 pp 1–12, DOI 10.2514/6.2022-1526
28. Jelloian CC, Bendana FA, Wei C, Spearrin RM, MacDonald ME (2022) Nonequilibrium Vibrational, Rotational, and Translational Thermometry via Megahertz Laser Absorption of CO. Journal of Thermophysics and Heat Transfer 36(2):266–275, DOI 10.2514/1.T6376, URL https://arc.aiaa.org/doi/10.2514/1.T6376
29. Jelloian C, Minesi NQ, Spearrin RM (2022) High-speed interband cascade laser absorption sensor for multiple temperatures in CO2 rovibrational non-equilibrium. In: AIAA SCITECH 2022 Forum, American Institute of Aeronautics and Astronautics, Reston, Virginia, pp 2022–2398, DOI 10.2514/6.2022-2398, URL https://arc.aiaa.org/doi/10.2514/6.2022-2398
30. Nair AP, Minesi NQ, Jelloian C, Kuenning NM, Spearrin RM (2022) RF-waveform optimization for MHz-rate DFB laser absorption spectroscopy in dynamic combustion environments. AIAA Science and Technology Forum and Exposition, AIAA SciTech Forum 2022 pp 1–13, DOI 10.2514/6.2022-2373
31. Hanson RK, Spearrin RM, Goldenstein CS (2016) Spectroscopy and Optical Diagnostics for Gases. Springer International Publishing, Cham, DOI 10.1007/978-3-319-23252-2
32. McLean A, Mitchell C, Swanston D (1994) Implementation of an efficient analytical approximation to the Voigt function for photoemission lineshape analysis. Journal of Electron Spectroscopy and Related Phenomena 69(2):125–132, DOI 10.1016/0368-2048(94)02189-7
33. Rothman L, Gordon I, Barber R, Dothe H, Gamache R, Goldman A, Perevalov V, Tashkun S, Tennyson J (2010) HITEMP, the High-Temperature Molecular Spectroscopic Database. Journal of Quantitative Spectroscopy and Radiative Transfer 111(15):2139–2150, DOI 10.1016/j.jqsrt.2010.05.001
34. Gordon I, Rothman L, Hargreaves R, Hashemi R, Karlovets E, Skinner F, Conway E, Hill C, Kochanov R, Tan Y, Wcisło P, Finenko A, Nelson K, Bernath P, Birk M, Boudon V, Campargue A, Chance K, Coustenis A, Drouin B, Flaud J, Gamache R, Hodges J, Jacquemart D, Mlawer E, Nikitin A, Perevalov V, Rotger M, Tennyson J, Toon G, Tran H, Tyuterev V, Adkins E, Baker A, Barbe A, Canè E, Császár A, Dudaryonok A, Egorov O, Fleisher A, Fleurbaey H, Foltynowicz A, Furtenbacher T, Harrison J, Hartmann J, Horneman V, Huang X, Karman T, Karns J, Kassi S, Kleiner I, Kofman V, Kwabia–Tchana F, Lavrentieva N, Lee T, Long D, Lukashevskaya A, Lyulin O, Makhnev V, Matt W, Massie S, Melosso M, Mikhailenko S, Mondelain D, Müller H, Naumenko O, Perrin A, Polyansky O, Raddaoui E, Raston P, Reed Z, Rey M, Richard C, Tóbiás R, Sadiek I, Schwenke D, Starikova E, Sung K, Tamassia F, Tashkun S, Vander Auwera J, Vasilenko I, Vigasin A, Villanueva G, Vispoel B, Wagner G, Yachmenev A, Yurchenko S (2022) The HITRAN2020 molecular spectroscopic database. Journal of Quantitative Spectroscopy and Radiative Transfer 277:107949, DOI 10.1016/j.jqsrt.2021.107949
35. Hargreaves RJ, Gordon IE, Rey M, Nikitin AV, Tyuterev VG, Kochanov RV, Rothman LS (2020) An Accurate, Extensive, and Practical Line List of Methane for the HITEMP Database. The Astrophysical Journal Supplement Series 247(2):55, DOI 10.3847/1538-4365/ab7a1a, URL https://iopscience.iop.org/article/10.3847/1538-4365/ab7a1ahttp://arxiv.org/abs/2001.05037
36. Gamache RR, Vispoel B, Rey M, Nikitin A, Tyuterev V, Egorov O, Gordon IE, Boudon V (2021) Total internal partition sums for the HITRAN2020 database. Journal of Quantitative Spectroscopy and Radiative Transfer 271:107713, DOI 10.1016/j.jqsrt.2021.107713, URL https://doi.org/10.1016/j.jqsrt.2021.107713https://linkinghub.elsevier.com/retrieve/pii/S0022407321002065
37. York D, Evensen NM, Martinez ML, De Basabe Delgado J (2004) Unified equations for the slope, intercept, and standard errors of the best straight line. American Journal of Physics 72(3):367–375, DOI 10.1119/1.1632486, URL http://aapt.scitation.org/doi/10.1119/1.1632486

38. BALTER-PETERSON A, NICHOLS F, MIFSUD B, LOVE W (1992) Arc jet testing in NASA Ames Research Center thermophysics facilities. In: AlAA 4th International Aerospace Planes Conference, American Institute of Aeronautics and Astronautics, Reston, Virigina, December, DOI 10.2514/6.1992-5041, URL https://arc.aiaa.org/doi/10.2514/6.1992-5041
39. Bendana FA, Lee DD, Spearrin RM, Schumaker SA, Danczyk SA (2019) Infrared laser absorption thermometry and CO sensing in high-pressure rocket combustion flows from 25 to 105 bar. In: AIAA Scitech 2019 Forum, American Institute of Aeronautics and Astronautics, January, DOI 10.2514/6.2019-1610
40. Bendana FA (2020) Shock tube kinetics and laser absorption diagnostics for liquid- and hybrid- propellant rocket combustion analysis. PhD thesis, University of California, Los Angeles
41. Campbell MF, Owen KG, Davidson DF, Hanson RK (2017) Dependence of Calculated Postshock Thermodynamic Variables on Vibrational Equilibrium and Input Uncertainty. Journal of Thermophysics and Heat Transfer 31(3):586–608, DOI 10.2514/1.T4952
42. Park C, Howe JT, Jaffe RL, Candler GV (1994) Review of chemical-kinetic problems of future NASA missions, II: Mars entries. Journal of Thermophysics and Heat Transfer 8(1):9–23, DOI 10.2514/3.496
43. Millikan RC, White DR (1963) Systematics of Vibrational Relaxation. The Journal of Chemical Physics 39(12):3209–3213, DOI 10.1063/1.1734182
44. Goodwin DG, Moffat HK, Speth RL (2018) Cantera: An object-oriented software toolkit for chemical kinetics, thermodynamics, and transport processes. DOI 10.5281/zenodo.170284
45. Johnston C, Brandis A (2014) Modeling of nonequilibrium CO Fourth-Positive and CN Violet emission in CO 2 –N 2 gases. Journal of Quantitative Spectroscopy and Radiative Transfer 149:303–317, DOI 10.1016/j.jqsrt.2014.08.025, URL http://dx.doi.org/10.1016/j.jqsrt.2014.08.025https://linkinghub.elsevier.com/retrieve/pii/S0022407314003690
46. Petersen EL, Hanson RK (2006) Measurement of Reflected-shock Bifurcation Over a Wide Range of Gas Composition and Pressure. Shock Waves 15(5):333–340, DOI 10.1007/s00193-006-0032-3
47. Li Y, Wang S, Strand CL, Hanson RK (2020) Two-temperature Collisional-radiative Modeling of Partially Ionized O 2 –Ar Mixtures over 8000–10,000 K Behind Reflected Shock Waves. The Journal of Physical Chemistry A 124(19):3687–3697, DOI 10.1021/acs.jpca.0c00466, URL https://dx.doi.org/10.1021/acs.jpca.0c00466https://pubs.acs.org/doi/10.1021/acs.jpca.0c00466
48. Li Y, Wang Y, Davidson DF, Hanson RK (2021) Collisional excitation kinetics for O(3s S o 5) and O(3p P3 5) states using laser absorption spectroscopy in shock-heated weakly ionized O2 -Ar mixture. Physical Review E 103(6):1–15, DOI 10.1103/PhysRevE.103.063211
49. Campbell MF, Wang S, Goldenstein CS, Spearrin RM, Tulgestke AM, Zaczek LT, Davidson DF, Hanson RK (2015) Constrained reaction volume shock tube study of n -heptane oxidation: Ignition delay times and time-histories of multiple species and temperature. Proceedings of the Combustion Institute 35(1):231–239, DOI 10.1016/j.proci.2014.05.001, URL http://dx.doi.org/10.1016/j.proci.2014.05.001https://linkinghub.elsevier.com/retrieve/pii/S1540748914000042
50. Coleman HW, Steele WG (2009) Experimentation, Validation, and Uncertainty Analysis for Engineers, 3rd edn. John Wiley & Sons, Inc., Hoboken, NJ, USA
51. Girard JJ, Hanson RK (2017) Minimally intrusive optical probe for in situ shock tube measurements of temperature and species via tunable IR laser absorption. Applied Physics B 123(11):264, DOI 10.1007/s00340-017-6840-6, URL https://linkinghub.elsevier.com/retrieve/pii/S001021801730007Xhttp://link.springer.com/10.1007/s00340-017-6840-6
52. Goldenstein CS, Schultz IA, Jeffries JB, Hanson RK (2013) Two-color absorption spectroscopy strategy for measuring the column density and path average temperature of the absorbing species in nonuniform gases. Applied Optics 52(33):7950–7962, DOI 10.1364/AO.52.007950